Rotary friction welding applied to Cu11.8Al0.45Be shape memory alloy

A.A.De Albuquerque, Hervé Louche, D. F. De Oliveira, I. C. A. Brito

Journal of Advanced Joining Processes 10 (2024) 100233

Contents lists available at ScienceDirect

Journal of Advanced Joining Processes

journal homepage: www.sciencedirect.com/journal/journal-of-advanced-joining-processes

Rotary friction welding applied to Cu11.8Al0.45Be shape memory alloy

A.A.de Albuquerque [a], H. Louche [b], D.F.de Oliveira [c], I.C.A. Brito [c,*]

[a] Department of Mechanical Engineering, Federal University of Paraíba, João Pessoa, PB, 58051-900, Brazil
[b] LMGC, CNRS, University of Montpellier, Montpellier, France
[c] Department of Materials Engineering, Federal University of Paraíba, João Pessoa, PB, 58051-900, Brazil

ARTICLE INFO

Keywords:
CuAlBe SMAs
Rotary friction welding
Welding zone
Welding microstructure
Mechanical properties
Martensitic transformation

ABSTRACT

The feasibility of welding a CuAlBe SMA by continuous drive friction welding was evaluated. The metallurgical state (annealed/quenched) before welding and frictional pressure (5 and 10 MPa) were varied and their effects on joint quality were analyzed. Static tensile tests, microhardness, thermal analysis by DSC, and optical microscopy were carried out to characterize the welded joint. The results indicated joints of excellent thermo-mechanical quality. The welding zones are well-defined, narrow, and have a very refined microstructure compared to the base metal. The phase transition temperatures along the welded assemblies were not changed when welding was performed on the quenched samples, except in the welding zone of the sample welded with 10 MPa. Maximum tensile strength was obtained by using maximum friction pressure during welding of the annealed alloy (quenching after welding). To fill the gap in bibliographical research in this field of study, this work innovatively presents the possibility of welding Cu-based SMAs by rotary friction, including the welding of quenched parts without the need for subsequent heat treatments and without compromising the shape memory effect.

Introduction

The industrial production of mechanical components may require welding at some manufacturing stage. Complex geometries such as turbine blades can be obtained by welding (Li et al., 2016), avoiding complex and costly machining operations. Welding techniques that produce the union through forming a molten pool, such as TIG, MIG/-MAG, laser (Oliveira et al., 2018), etc., generally produce defects characteristic of metal solidification. These defects include porosity, oxide inclusions, and hot cracks to large distortions caused by residual stresses (Oliveira et al., 2017). Furthermore, the highly localized heat input produces large thermally affected zones, which, depending on the type of material, can produce major microstructural changes and mechanically compromise the joint.

When high reliability of the welded joint is required with minimal microstructural changes, whether in the welding zone (WZ) or in the thermally affected zone (TAZ), the use of rotary friction welding (RFW) may be an option (Li et al., 2016; Vairis et al., 2016; Shinoda et al., 1992). Easy to automate, its variants allow welding in the solid state and can be adapted for welding a wide range of dimensions and materials. The presence of a narrow WZ is one of the main advantages of this technique. (Vairis et al., 2016; Fukumoto et al., 2010; Ramesh Kumar et al., 2023; Rehman et al., 2021a, 2021b; Vyas et al., 2022; Preuss et al., 2004; Taheri et al., 2019; Damodaram et al., 2013; Zhang et al., 2022; Turner et al., 2012; Karadge et al., 2008). However, the choice of appropriate process parameters for each type of material, such as rotation, friction pressure, forging pressure, welding time, etc., is extremely important (Li et al., 2016; Vairis et al., 2016; Shinoda et al., 1992; Uday et al., 2010; Shinoda et al., 1999).

RFW can be divided into two variants: continuous drive (CDFW) and inertial variant (IFW). In CDFW, the thermal input required for welding and the high rates of deformation are obtained by a motor/reducer system. With limited power, this process is generally used to weld small cross-sections. In IFW, the energy required for welding is stored in a flywheel in the form of kinetic energy, released both in thermal energy and plastic deformation in the WZ until the system stops (Li et al., 2016; Uday et al., 2010). The process CDFW is basically controlled by rotation speed (ω) and friction pressure (P_f) which play an important role in the quality of the joint. It can be said that the increase in ω causes greater heat generation and shorter welding time. Similarly, P_f is directly related to the rate of flash formation, which is the part of the material that flows due to high temperature and pressure. In industrial practice, these

* Correspondent author.
E-mail address: ieverton.brito@academico.ufpb.br (I.C.A. Brito).

https://doi.org/10.1016/j.jajp.2024.100233

Available online 11 June 2024

variables are selected together to result in a smaller TAZ.

The average rate of heat generation during welding of a cylindrical sample of radius R can be estimated by the equation $\dot{q} = (2/3)\pi R^3 \mu P_f \omega$ where μ is the friction coefficient at the interface. If more precise values for $\dot{q}$ are required, the coefficient μ, considered constant in the previous equation, must be admitted as a function of important parameters in the process (Li et al., 2016). In the mechanics of materials, friction welding (FW) can be considered a forging process involving high deformation rates at high temperatures, with the highly deformed region having a narrow width. The microstructural analysis of friction-welded components indicates the presence of three distinct regions depending on the deformations and temperatures to which they were subjected during welding. Briefly, they can be defined and characterized as (1) welding zone (WZ), a well-defined region subject to solid-state transformations and characterized by a refined microstructure of recrystallized grains; (2) thermomechanically affected zone (TMAZ), region subjected to moderate/low plastic deformation, temperature, and dynamic recrystallization in appropriate conditions; (3) base metal (BM), region subjected to low-temperature levels where no microstructural or mechanical changes are observed due to low thermal input (Li et al., 2016; Oliveira et al., 2017; Uday et al., 2010; Prabu et al., 2023).

Based on the need to obtain more efficient and sustainable manufacturing routes, the use of FW of SMAs is widely studied. However, its use remains restricted to NiTi SMAs whether in joints of similar or dissimilar materials (Shinoda et al., 1992; Fukumoto et al., 2010; Rehman et al., 2021a, 2021b, 2021c; Shinoda et al., 1999; Mani Prabu et al., 2017; Mani Prabu et al., 2019; West et al., 2021). After appropriate heat treatment, SMAs present shape memory effect (SME) thanks to a reversible martensitic transformation. In free-stress conditions, a thermal cooling can convert austenite into martensite at a starting temperature M_s and an ending temperature M_f (called direct transformation - exothermic). The reverse transformation (M → A), endothermic, starts at temperature A_s and ends at A_f (Montecinos and Cuniberti, 2008). The behavior of these transformations is strongly dependent on the chemical composition, microstructure, and processing history as the latter introduces microstructural defects in the material (Dunne et al., 2004; Roca et al., 2017; Kaouache et al., 2004; Cuniberti et al., 2009). At the end of processing, if the transition temperatures have been considerably altered, the component may become unusable due to the loss of its functional characteristics.

Microstructure and residual stresses tend to interfere with phase transition temperatures (PTTs) (Roca et al., 2017; Sun et al., 2014; Mazzer et al., 2017). Thus, some simple thermodynamic parameters can be used to detect changes in the behavior of the martensitic transformation depending on the material's processing history. Thermomechanical cycles imposed during processing tend to introduce crystallographic defects (vacancy and dislocations) that delay the transformation. This delay is related to the elastic energy stored in the vicinity of these defects (da Silva Andrade et al., 2021; Mazzer et al., 2015). High values of ($|A_f - A_s|$ or $|M_f - M_s|$) indicate a high density of defects while hysteresis ($A_s - M_f$) is related to the surface energy dissipated in the transformation. Thus, more refined microstructures tend to present higher values of ($A_s - M_f$) due to the high density of grain boundaries (Roca et al., 2017; da Silva Andrade et al., 2021; Zu et al., 2002).

In this sense, this work aimed to study the feasibility of welding a CuAlBe SMA by CDFW, something not yet presented in the literature. After welding and appropriate characterizations, the technique may be considered viable if the joints have tensile strength compatible with BM and do not present significant variations in microstructure and PTTs. Welding the quenched alloy opens the possibility of producing components using CuAlBe SMAs in a more ecological and viable way, making heat treatment steps in large parts easier. Furthermore, if SME is desired in some parts of a device or machine element, only the parts of interest can be joined by FW. Therefore, systems for seismic damping (Ozbulut et al., 2007) and fixing (de Oliveira et al., 2017; da Paz et al., 2022) can be manufactured by WF using simpler and more sustainable routes.

To assess the joining efficiency, this study conducted exploratory scanning calorimetry analysis to evaluate PTTs, microstructural analysis, microhardness testing, and tensile tests. Two values of P_f and metallurgical states (annealed and quenched) were applied before welding, and their effects were evaluated. The investigation into welding in the quenched state is particularly significant, as it offers the potential for manufacturing complex geometry components by welding smaller parts, thus facilitating more manageable and cost-effective heat treatment procedures.

Experimental procedures

Cu-11.8Al-0.45Be (wt.%) SMA was obtained from high-purity copper and aluminum and the master alloy Cu-10Be (wt.%). The melting took place by induction (Make: INDUTHERM, Type: MU400), without atmosphere control and in a graphite crucible, followed by pouring from 1200ºC into a SAE1020 steel mold, as indicated in Fig. 1(a). All ingots, Fig. 1(b), were chemically homogenized for 4 h at 850ºC (Make: SP Labor, Type: 8P-1200DM/C) without atmosphere control.

After chemical homogenization and still at 850ºC, the ingots were divided into 3 groups according to the cooling conditions and the sequence adopted for welding and quenching, as described below. 1st group (called Quenched After Welding [QAW]) - slow cooling (~ 0.75ºC/min) inside the furnace to room temperature (~25ºC) → welding → quenching; 2nd group (called Welded After Quenched [WAQ]) - quenching in water (850ºC → 25ºC) → welding; and the 3rd group - quenching in water (850ºC → 25ºC) no welding (a condition called Reference).

The methodology used in this work aims to evaluate the thermomechanical behavior of the material welded under different metallurgical states: quenched (the alloy already has the SME) and annealed (the SME will be obtained after quenching the welded assembly) and compared with the results obtained for the unwelded alloy (called Reference). After identification, the ingots to be welded were conventionally machined in the form of cylinders with dimensions Ø11.6 mm x 30 mm, as indicated in Fig. 1(c). The surfaces to be welded were machined by turning using strictly the same machining parameters and the use of lubrication/cooling. The objective of extreme care in machining the surfaces was due to the coefficient of friction between the surfaces being dependent on the surface roughness (Sedlaček et al., 2009) and being altered by the cutting parameters (Qehaja et al., 2015; Abburi and Dixit, 2006; Del Sol et al., 2019).

The system used in this work to weld the samples by CDFW was obtained by adapting a milling machine (Make: SINITRON, Type: ISO 30), as shown in Fig. 2. The motor shaft is released to move vertically with a constant rotation speed of 1500RPM, Fig. 2(a). The compression forces are produced by a lever system. A known weight is positioned at position L10 of the lever to produce friction pressure of 10 MPa and

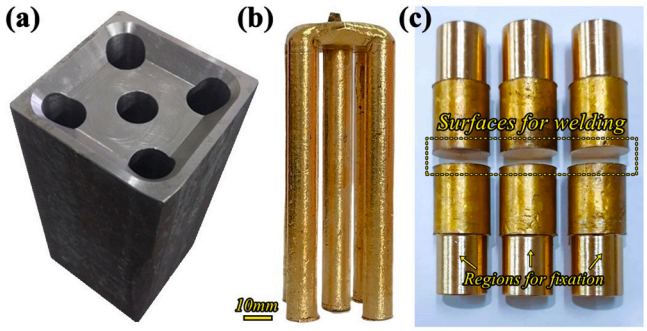

Fig. 1. SAE 1020 steel metallic mold (a), ingot in the "as-cast" condition (b), and pre-machined ingots before the welding stage (c).

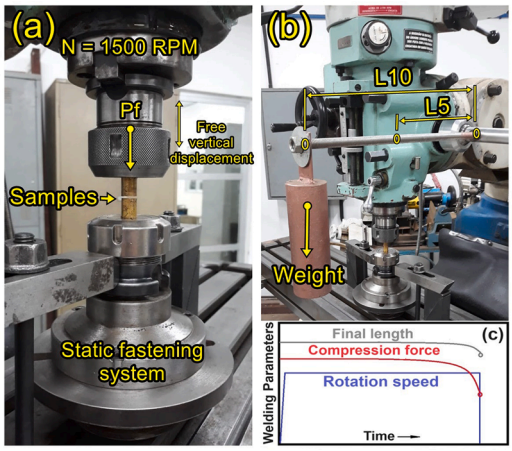

Fig. 2. Samples fixed on the motor shaft and static support (a), lever system to obtain the desired friction pressure (b), and behavior of welding parameters over time (c).

moved to position L5 to produce 5 MPa, as indicated in Fig. 2(b). The formation of the flash results in the shortening of the samples and the displacement of the shaft downwards, resulting in a small rotation in the lever. Thus, the compression force can be considered constant until the beginning of shortening, this force decreases then slightly in the final welding step as shown in the diagram in Fig. 2(c). Tests carried out before carrying out this work indicated reductions in the compression force not greater than 20 %.

Two values of P_f were evaluated during welding, 5 MPa and 10 MPa, resulting in axial compression loads of ~540 N and ~1080 N, respectively. The parameter established for taking the time required for welding was the prior "slippage" of the equipment's belt transmission system during welding. After the assembly is welded, the drive shaft is stopped abruptly. In the end, four conditions were evaluated: Welded After Quenching with P_f = 10 MPa – **[WAQ-10]**, Welded After Quenching with P_f = 5 MPa – **[WAQ-5]**, Quenching After Welded with P_f = 10 MPa – **[QAW-10]**, and Quenching After Welded with P_f = 5 MPa – **[QAW-5]**.

For each studied condition, a sample was evaluated by optical microscopy (OM) and Vickers microhardness. The welded assembly was machined in the form of a cylinder with Ø 10 mm and then ground until reaching the diametral longitudinal plane, as shown in Fig. 3(a). After this, the samples were properly metallographically prepared and attacked in an aqueous solution of ferric chloride (10 g of $FeCl_3{\cdot}6H_2O$ in 90 ml of distilled H_2O) and analyzed by OM (Make: OLYMPUS, Type: BX41M). The aluminum support shown in Fig. 3(a) aims to ensure perpendicularity during microhardness and OM analyses. The average grain size (GS) was measured using the linear intercept method. XRD analyses (BRUKER, Type: D8 Discover) were carried out in 20–100º 2theta (step 0.033º) using Cu-Kα radiation (λ = 1.5418 Å) with 40KV and 40 mA. The regions analyzed were the WZs with ~ Ø6mm.

To evaluate the Vickers microhardness (Make: SHIMADZU, Type: HMV-2) profile along the WZ and TMAZ, indentations were made (load: 4.9 N, time: 15 s) at every 1 mm and in 3 lines (L1, L2 and L3). The length of each line measures 30 mm and the spacing between lines was 2.5 mm (position $x = -15$ mm to $x = 15$ mm), as indicated in Fig. 1(a). Uniaxial tensile tests (Make: SHIMADZU, Type: AUTOGRAPH AG – X 10KN) were carried out at a temperature of 25ºC, loading speed of 0.5 $mm.min^{-1}$, and preload of 20 N on 5 samples with the configuration indicated in Fig. 3(b). The displacements were measured exclusively by the testing machine itself, without additional extensometry.

Only conditions [WAQ-10] and [WAQ-5] were evaluated by differential scanning calorimetry – DSC (Make: SHIMADZU, Type: DSC-60), to evaluate the behavior of martensitic transformation after welding. For each condition, samples with Ø 4.5 mm x 1.5 mm (~170 mg) were taken

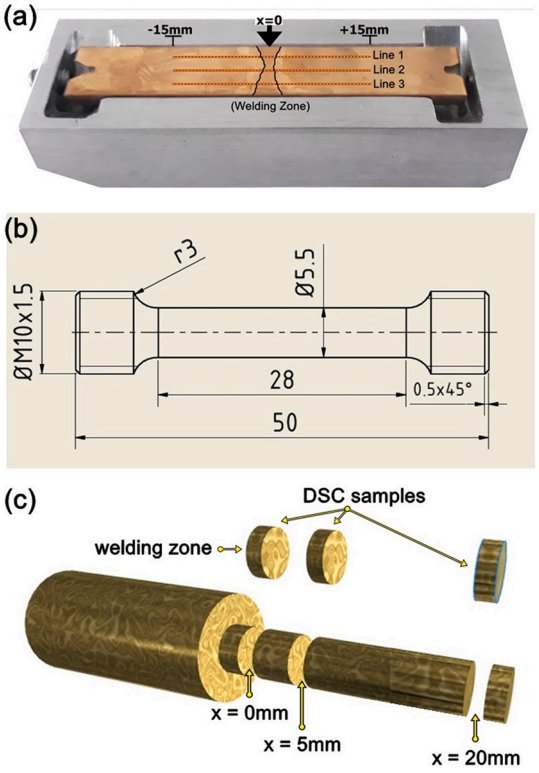

Fig. 3. Configuration adopted for evaluation of the Vickers microhardness profile and OM analysis (a), uniaxial tensile test samples, dimensions in (mm) (b), and positions evaluated by DSC (c).

from the positions: $x = 0$ mm (WZ), $x = 5$ mm, and $x = 20$ mm, as shown in Fig. 3(c). The thermal analysis was carried out under an N_2 atmosphere with a flow rate of 50 ml/min, and a heating/cooling rate of 10ºC/min in the temperature range of 50 to 480ºC, in two cycles. The second cycle was considered for analysis.

Results and discussion

Analysis of the time for welding and axial reduction

Fig. 4 shows the characteristics of flash obtained during CDFW. After a thorough visual inspection, it was not possible to verify any differences between the characteristics of the flash depending on the metallurgical state or the level of pressure applied. To achieve this, we chose to determine the total reduction in length generated during welding, since

Fig. 4. Cu-11.8Al-0.45Be SMA welded by CDFW and flash characteristics.

the volume reduced by the shortening of the initial samples (cylindrical geometries) corresponds to the volume of the flash formed.

Table 1 shows the average time required for welding and the average final length measured in 10 samples for each condition studied in this work. The data indicates that $P_f = 10$ MPa produces the shortest welding times despite not producing the largest axial reductions. This behavior can be explained by the higher rate of heat generation at the union interface as friction forces increase, resulting in high and sudden heating in a narrow region of the interface (Li et al., 2016; Oliveira et al., 2017; Uday et al., 2010; Prabu et al., 2023). The small volume of superheated material flows plastically under the action of the compressive load and results in a less pronounced flash.

For the [WAQ] condition, the use of $P_f = 5$ MPa resulted in an average welding time of ~2.5x compared to $P_f = 10$ MPa, while for the [QAW] condition this value was ~1.8x. Table 1 shows that the welding time is not strongly influenced by the metallurgical state for the case of $P_f = 10$ MPa, while for $P_f = 5$ MPa the annealed alloy presents a reduction of ~25 % in the welding time compared to the quenched alloy. We suggest three characteristics that contribute to explaining this reduction in welding time between conditions [QAW-5] and [WAQ-5].

1. The annealed samples present a microstructure composed of α (ductile) and γ_2 (brittle) phases after slow cooling from the betatization temperature (850ºC) (Canbay et al., 2021; Kök et al., 2018; Ponweiser et al., 2011; Zhang et al., 2023). This produces a tribological condition with a higher μ compared with martensitic samples. As heat generation is directly proportional to μ, higher heat generation rates are produced in the [QAW] condition. The difference in microhardness of the annealed (209.9 ± 5.7 HV) and quenched (181.7 ± 11.0 HV) alloy supports this hypothesis. Fig. 5 shows the microstructures and microhardness profile resulting from welding martensite (quenched alloy) / (α + γ_2) (annealed alloy) by CDFW (P_f=10 MPa).
2. Ongoing and not yet published results show that the thermal conductivity of the annealed sample seems relatively lower than the conductivity of the quenched sample. This hinders the conductive flow of heat through the sample, resulting in higher temperatures in the lower conductivity sample [QAW] compared to the higher thermal conductivity sample [WAQ].
3. As the samples in the [WAQ] condition already have SME before welding, the heating generated by friction between the faces of the samples thermally induces the reversible martensitic transformation (M→A). This endothermic transformation ($\Delta H^{M\rightarrow A} = 57$ MJ/m^3) starts around 180ºC (see item 3.4) for almost all samples. As the heating rates produced during welding are very high, contrary to what occurs in a DSC analysis, it is assumed that the transformation must occur quickly, with rapid energy absorption and an abrupt decrease in local temperature. This cooling would contribute to an increase in welding time in the [WAQ] condition compared to the [QAW] condition.

For the same P_f, the greatest shortenings were observed for the [WAQ] condition. We can justify this behavior using the hypothesis that heat diffuses easily through martensitic samples [WAQ] due to their greater thermal conductivity and this results in a superheated volume that will flow more easily under the action of P_f (Li et al., 2016; Uday et al., 2010). For the same metallurgical state, $P_f = 5$ MPa produces greater shortening by allowing the overheating of a larger volume of material since the welding time required for welding is considerably longer compared to $P_f = 10$ MPa.

Table 1
Time required for CDFW welding and shortening after welding.

	WAQ-10	*WAQ-5*	*QAW-10*	*QAW-5*
Time for Welding (s)	17 ± 1	43 ± 20	18 ± 4	32 ± 14
Final Length (mm)	56.8 ± 2.3	55.0 ± 1.5	57.5 ± 2.3	56.9 ± 1.9
Shortening (%)	5.3 ± 3.9	8.3 ± 2.4	4.2 ± 3.8	5.1 ± 3.1

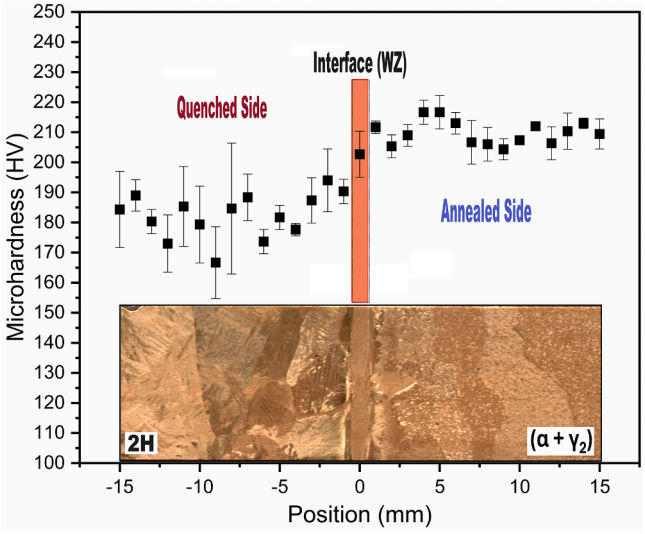

Fig. 5. Microstructures and microhardness profile for the dissimilar joint obtained by CDFW (P_f = 10 MPa) for a quenched and annealed Cu-11.8Al-0.45Be alloy.

Analysis of the welding zone by XRD

The electron/atom ratio (e/a) is a parameter widely used to predict the type of martensite to be obtained depending on the atomic fractions and valence of the elements that make up the alloy. It is established that values of e/a lower than 1.45 result in a monoclinic 18R martensite while values greater than 1.49 imply a hexagonal 2H martensite. Thus, e/a values between 1.45 and 1.49 result in the coexistence of phases 18R and 2H. As e/a approaches 1.45 or 1.49, the proportions of 18R and 2H tend to increase, respectively (Canbay et al., 2021, 2020). Despite being calculated based on the real concentration of each element in the alloy, $e/a = 1.4949$ calculated from the nominal composition (73.92Cu-23.41Al-2.67Be (at.%)) suggests the predominance of martensite of type 2H in our case. The diffractograms for all conditions studied including the alloy slowly cooled in the furnace to room temperature (annealed sample - Sample A) are shown in Fig. 6 for comparison purposes.

Fig. 6 indicates that the slowly cooled alloy is effectively composed of (α + γ_2) as predicted by the CuAl equilibrium diagram (Chentouf et al., 2010; Pushin et al., 2022). The reference presents 2H-type martensite with a small amount of (α + γ_2) not identifiable in optical microscopy analyses. The presence of equilibrium phases probably comes from the slower cooling in the central region of the samples during quenching and where the X-ray diffraction analyses were carried out. The samples quenched after welding (QAW) also presented equilibrium phases in negligible proportions. In the case of samples welded after quenching [WAQ], the intensity of the peaks referring to the α and γ_2 phases is higher, suggesting the presence of a greater quantity of both phases concerning the reference and [QAW]. XRD analyses were carried out in a Ø 6 mm region on the WZ. Due to the great difference in textures in this region, the determination of the volumetric fractions of these phases was not calculated.

Chentouf et al. (2010) evaluated the precipitation of (α + γ_2) in the Cu-11.4Al-0.52Be alloy (wt.%) subjected to aging at 350ºC. The authors observed that precipitation only started after 140Ks. Kuo et al. (2006) only observed precipitation of α and γ_2 from 20 h onwards at 200ºC in the Cu-10Al-0.8Be alloy (wt.%). Compared to the time intervals studied by Chentouf et al. and Kuo et al., the welding time for all conditions evaluated in this work is negligible. Therefore, it is possible that the

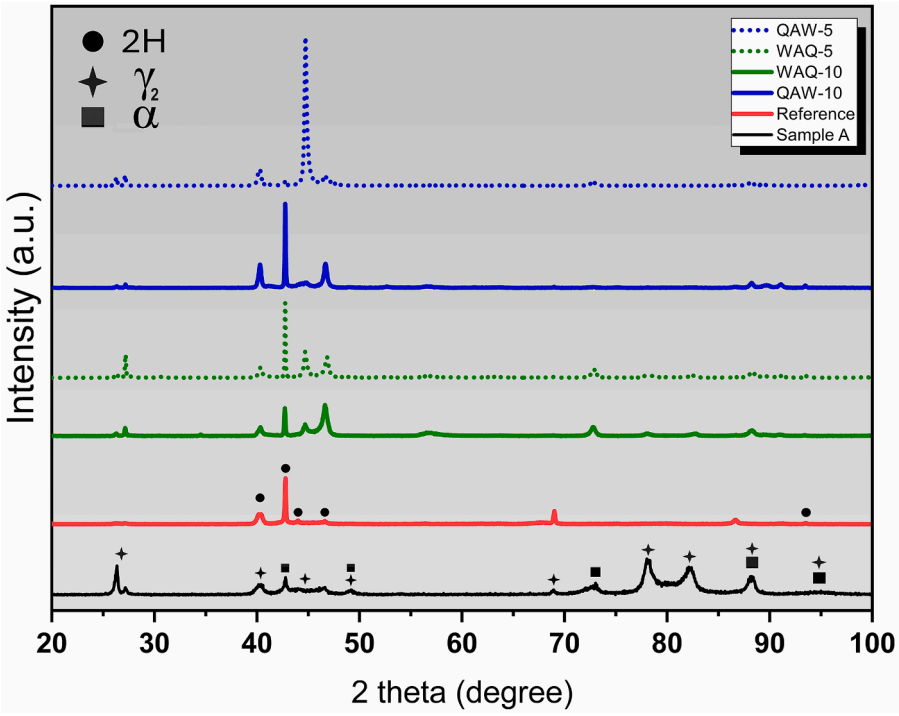

Fig. 6. X-ray diffractogram patterns of the Cu-11.8Al-0.45Be alloy welded by CDFW.

precipitation of the equilibrium phases in the [WAQ] condition was caused by the exposure of the material to high temperatures, which accelerates precipitation. Cuniberti et al. (2009) show that the nucleation of the γ_2 precipitates begins between (557 – 580ºC) followed by the growth stage and an increase in their volumetric fraction.

As the temperature behavior during the welding of the samples was not monitored, it is not possible to say which were the maximum temperatures reached and the time spent at these temperatures. However, it is possible to ensure that the exposure time to high temperatures is a few seconds (limited to the welding time) and, this slows down the growth of precipitates and the increase in the volumetric fraction in the martensitic matrix.

Analysis of the welding zone by optical microscopy

Fig. 7 shows the WZs for all conditions studied in this work. The black lines enhance the visualization of the WZ, which has an hourglass shape. This geometry results from the non-uniform temperature distribution along the welding surfaces and is caused by an increasing heat generation due to the increase in tangential speed from the center to the edge (S_{tang} ~ 900 mm/s) (Li et al., 2016). The thickness of the WZ for the [QAW] was larger compared to the [WAQ] due to the recrystallization and grain growth in the WZ promoted by the supply of energy during the pre-quenching stage (850ºC for 1 h).

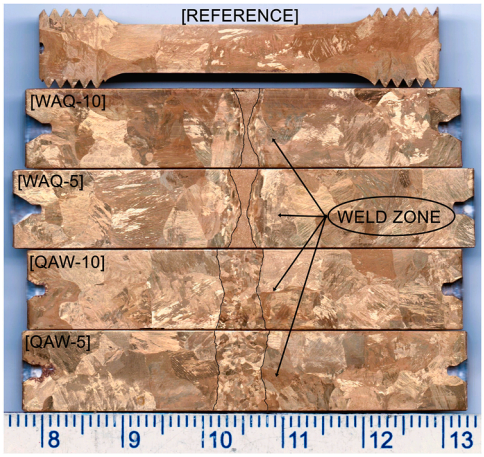

Fig. 7. Macrographs of base metal and samples welded by CDFW.

Despite the small irregularities in the WZ geometry shown in Fig. 7, it appears that the [WAQ-10] sample has a smaller WZ thickness (~300 μm) compared to the [WAQ-5] condition (~750 μm) measured in the center of the region (narrowest region). However, when measured on the edges of the samples (wide: ~10 mm), the thicknesses of the WZs presented values close to 2.88 mm for [WAQ-10] and 3.14 mm for [WAQ-5]. For the [QAW] conditions, the WZ was more uniform and measured ~5.9 mm for [QAW-10] and ~ 6.0 mm for [QAW-5]. The results obtained are consistent with the results of Ates et al. (2007) and Grant et al. (2009) who found that the width of the WZ increases with increasing P_f and ω in a particular way depending on the type of material. Grant et al. (2009) also state that low friction pressures make the extrusion stage of the plasticized material difficult and result in narrower WZ.

Fig. 8 shows the microstructures of the WZs for all conditions studied. Fig. 8(a) and (b) show the WZ / BM interface for the [WAQ] conditions and a narrow TMAZ, easily identified by the severely deformed grains. Comparison between Fig. 8(a) and (b) makes it clear that $P_f = 10$ MPa produced a wider TMAZ compared to ~~using~~ 5 MPa. It was not possible to determine by OM the precise widths of the TMAZ for the [WAQ] and no trace of this region was found in the [QAW] condition, Fig. 8(c-d).

The absence of a TMAZ in the [QAW] condition is due to the complete recrystallization of this region during the pre-quenching stage (1 h at 850ºC). Several studies show that short time intervals are sufficient to recrystallize the microstructure of plastically deformed alloys. Pedrosa et al. (2022) showed that the 1800s at 850ºC were sufficient to obtain a recrystallized microstructure of the hot-rolled CuAlBeNbNi alloy. Ozbulut et al. (2007) obtained recrystallization of the Cu11.8Al0.5Be alloy at 180 s upon heating to 700ºC. Freudenberger et al. (2010) stated that 1000s at 300ºC were sufficient to recrystallize the alloys CuAl5 and

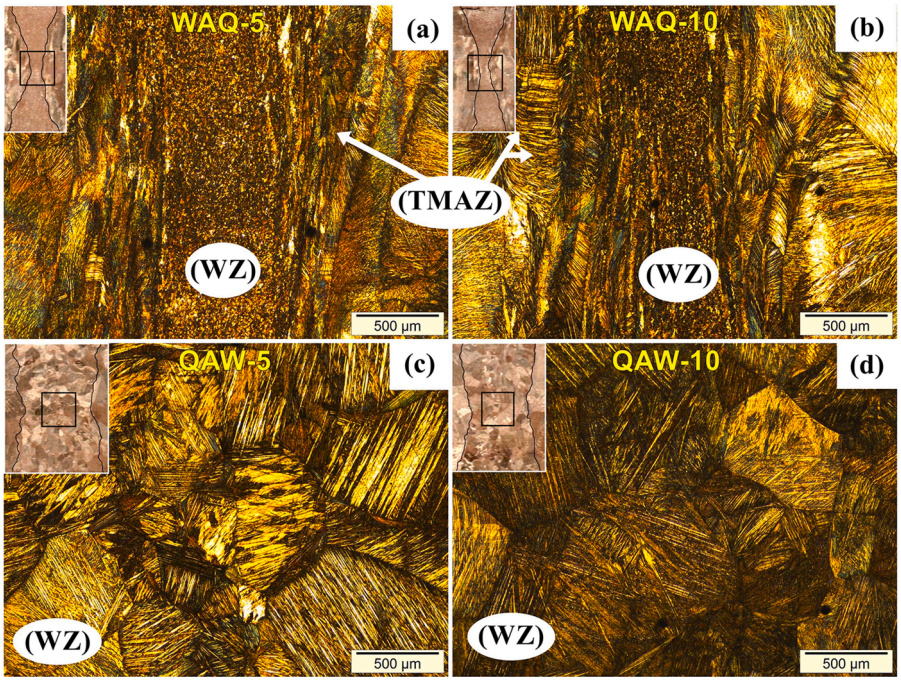

Fig. 8. OM images of the WZs for conditions [WAQ-5] (a), [WAQ-10] (b), [QAW-5] (c), and [QAW-10] (d) obtained from the central region of the WZ.

CuZn25 while Moghaddam et al. (2013) obtained total recrystallization of the alloys Cu-11Al5.6Mn and Cu-11.8Al-3.7Ni-1Mn in 15 s and 50 s, respectively.

The difference in GS in the WZs between the [QAWs] conditions is not easily seen by looking at Fig. 8. However, the use of the linear intercept method to calculate the GS (Moghaddam et al., 2013) in the WZ indicated an increase of ~26 % between [QAW-5] (492.1 ± 137.5 μm) and [QAW-10] (619.9 ± 86.2 μm). The increase in GS to a higher P_f value is associated with the exposure of sample [QAW-10] to a longer grain growth period compared to condition [QAW-5] during the pre-quenching stage (1 h at 850 °C).

The large number of dislocations generated during heating/cooling and severe plastic deformation introduce deformation energy into the material, favoring the recrystallization stage of the WZ (Andrade et al., 1994; Huang and Logé, 2016). The formation of numerous misoriented grains resulting from the rupture of grains from the base metal during welding also promotes recrystallization (Feng and Ma, 2009) and leads to microstructure refinement. Thus, the nucleation of new grains initiates more rapidly in samples subjected to higher P_f values. The GS of 10.8 ± 1 μm [WAQ-10] and 12.7 ± 1 μm [WAQ-5] confirms this hypothesis.

Fig. 9(a) shows the microstructure in the WZ for the [WAQ-10] case and Fig. 9(b) shows the interface WZ / plastically deformed martensitic grain that constitutes the TMAZ. This interface measured around 16 μm and extended on both sides along the entire WZ. The microstructure of the WZ obtained at 1000x magnification indicated in Fig. 9(b) shows the considerable difference between the GS on the two sides. The microstructure of the BM in our work (see Fig. 7.) can be considered extremely coarse and non-uniform concerning the microstructure of the WZs and when compared with the GS of CuAlBe alloys found in some works (0.04, 0.20, 0.50, 0.90 and 2.2 mm) (Montecinos and Cuniberti, 2014), (0.012 mm) (Roca et al., 2017), (0.5 mm) (Montecinos and Cuniberti, 2008) and (2 mm) (VHC de Albuquerque et al., 2010). This coarse microstructure is due to the absence of grain refiners and slow solidification in the metallic mold used.

Vickers microhardness

Fig. 10 shows the average microhardness (HV) profile measured along the welded samples, passing through the WZ ($x = 0$) (see Fig. 3

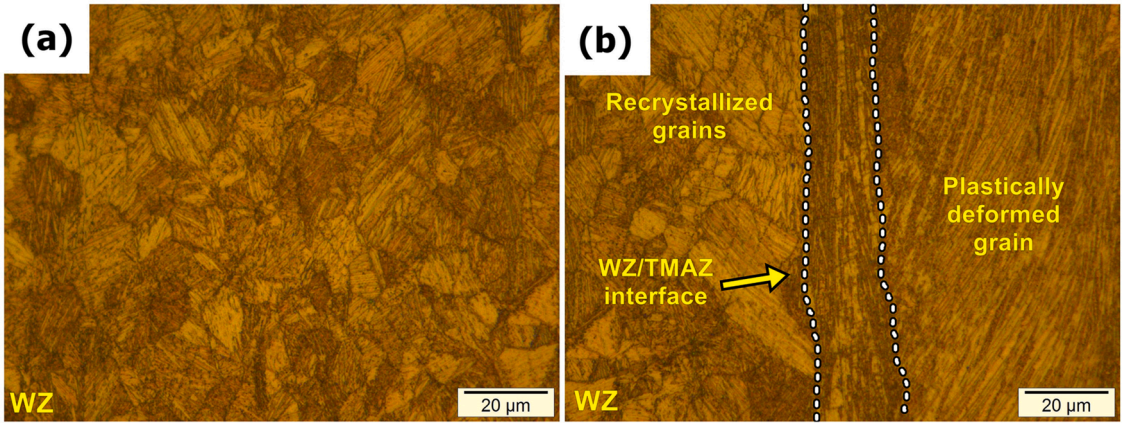

Fig. 9. Microstructure by OM of WZ (a) WZ/TMAZ interface (b). Condition [WAQ-10]. 1000x magnification.

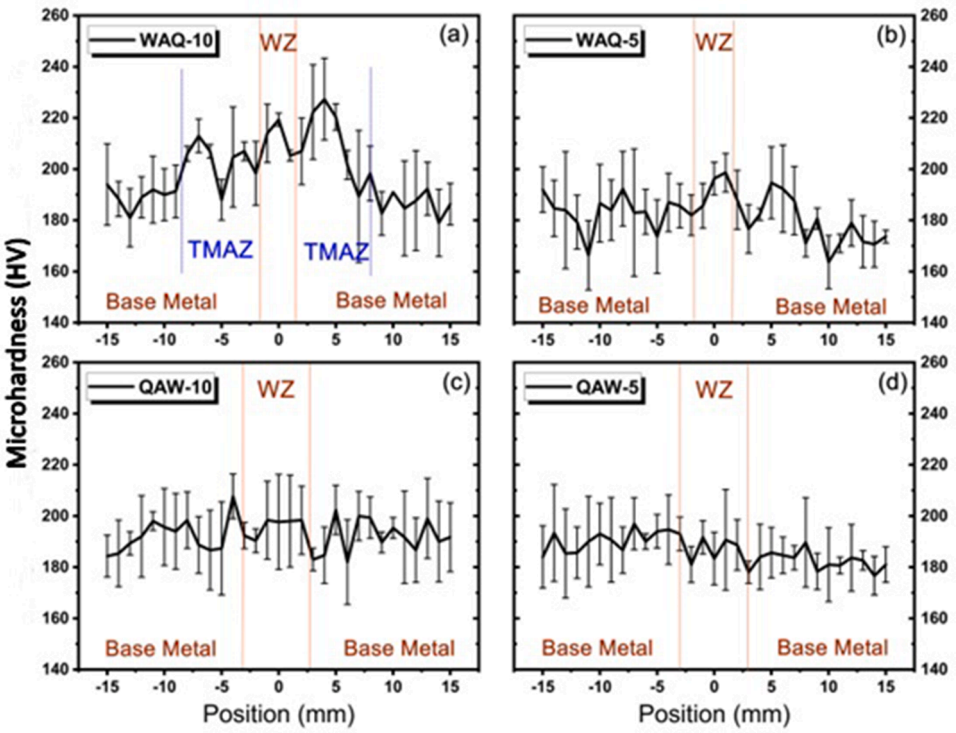

Fig. 10. Vickers microhardness profile along the position x=−15 mm to x = 15 mm for [WAQ] and [QAW] conditions.

(a)). For the [QAW-10] condition, the four practically uniform HV values (around $x = 0$) were measured within the WZ. The HV value of the 4 points (198 ± 16 HV) was slightly higher than the HV value measured in the reference (192 ± 11 HV) due to the smaller GS in the WZ. Several studies (Damodaram et al., 2013; Rehman et al., 2021c; Montecinos and Cuniberti, 2014; Bahador et al., 2019; Sampath, 2005; Silva et al., 2023) show the correlation of GS and HV. This relationship is given by the Hall-Petch relationship: $\sigma_Y = \sigma_0 + Kd^{-1/2}$ where σ_Y is the yield stress of the material with grain size d. K and σ_0 are material-dependent constants. In our case, the difference in HV between MB and WZ implies that the dependence of σ_Y on GS is not high.

[QAW-5] condition does not present the same uniformity in HV values in the WZ, probably due to greater dispersion in GS. Condition [QAW-5] presents a coefficient of variation of 27.94 % for GS while [QAW-10] has practically half this value (CV = 13.91 %). The high elastic anisotropy ratio of Cu-based SMAs (Xie et al., 2015) contributes to the dispersion in the values of mechanical properties, including HV in the WZ and BM. [WAQ-10] presented a region approximately ±8 mm wide around the WZ with high HV values and high dispersion in relation to the BM. As there is no noticeable difference in the GS of the BM in this region (see Fig. 7), the presence of ($\alpha + \gamma_2$) and residual stresses may have affected the microhardness behavior in the vicinity of WZ. Therefore, we will consider this region as a TMAZ. The slight reduction in HV in the sample [WAQ-5] compared to sample [WAQ-10] may be a consequence of a softening phenomenon caused by prolonged heating during welding (Priymak et al., 2020).

Martensitic transformation behavior

Only the [WAQ] condition was subjected to thermal analysis by DSC to evaluate the influence of CDFW on the martensitic transformation behavior. Samples [QAW] were not evaluated by DSC due to the complete recrystallization of the WZ as discussed in the previous section. The PTTs and the forward and reverse martensitic transformation curves of the (reference), [WAQ-10], and [WAQ-5] conditions are shown in Table 2.

Table 2
Phase transition temperatures (°C) and kinetic parameters of Cu11.8Al0.45Be (% wt.) SMA welded by CDFW.

Sample	Position (mm)	A_s	A_f	M_s	M_f	T_0	(A_s - M_f)	(M_s - M_f)
Reference	–	191	234	204	154	219	37	50
[WAQ-10]	$x = 0$	163	210	181	89	196	74	92
	$x = 5$	190	207	187	147	197	43	40
	$x = 20$	190	211	184	147	198	43	37
[WAQ-5]	$x = 0$	186	208	183	147	196	39	36
	$x = 5$	193	209	187	150	198	43	37
	$x = 20$	190	208	183	144	196	46	39

The values of hysteresis (A_s - M_f), (M_s - M_f), and PTTs at positions x = 5 and x = 20 mm of the sample [WAQ-10] were not changed by CDFW. Small differences can be attributed to inaccuracy in obtaining PTTs using the tangent method. The high microhardness values in the ±8 mm region (see Fig. 10(a)) attributed in part to possible residual stresses and precipitation of ($\alpha + \gamma_2$) were not sufficient to alter the behavior of the martensitic transformation at the x = 5 mm position. The increase in the density of crystallographic defects (mainly dislocations) can be qualitatively evaluated by the values of (M_s - M_f) and T_0. $T_0 = ½(M_s+A_f)$ is the temperature at which the Gibbs free energy of the forward and reverse transformations is equal to zero (da Silva Andrade et al., 2021). The high values of T_0 and (M_s – M_f) for the reference and [WAQ-10, x = 0] compared to the other conditions studied in this work indicate the strong presence of microstructural defects.

For the reference condition, the defects arise from sudden cooling during quenching (Dunne et al., 2004; Mazzer et al., 2015; Sampath et al., 2020). For [WAQ-10, x = 0], the high density of defects arises from the severe plastic deformation and the intense heating/cooling cycle in this region (Huang and Logé, 2016; Feng and Ma, 2009). [WAQ-10, x = 0] presents values of (M_s - M_f) approximately 2.3x higher than that obtained for [WAQ-10, x = 5] and ~2.5x for [WAQ-10, x = 20]. The lower M_f and A_s temperatures in this condition, Fig. 9(a), are justified as the stored elastic energy due to these defects acts as a barrier

to forward transformation and serves as a driving force for reverse transformation (Mazzer et al., 2017). Therefore, it is not possible to attribute the broadening of the transformation peaks observed in [WAQ-10, $x = 0$] to precipitation from the γ_2 phase since Cuniberti et al. (2009) show that even for a volumetric fraction of γ_2 of ~14 % the change in the PTTs is irrelevant ($\Delta M_s \sim 5$°C). Furthermore, the same authors demonstrate that an increase in the volumetric fraction of γ_2 tends to elevate the start and end temperatures of the direct and reverse transformations. In this study, only M_f and A_s were observed to decrease to lower values compared to the other conditions.

The sample [WAQ-5, $x = 0$] indicated in Fig. 11(b) does not present any anomaly in the heating/cooling curves as observed in [WAQ-10, $x = 0$]. It is assumed that prolonged heating during welding contributed to reducing the density of dislocations produced during welding (Priymak et al., 2020; Mazzer et al., 2017; Kaouache et al., 2004). It is worth noting that the difference in welding time between both conditions is greater than 2.5x. The increase in grain boundary density also modifies the martensitic transformation behavior (Roca et al., 2017). The parameter (A_s - M_f) qualitatively indicates the influence of the surface energy of the grain boundaries on the direct and reverse transformations. Thus, the increase in this parameter for the condition [QAW-10, $x = 0$] compared to [QAW-5, $x = 0$] can be attributed to a refined microstructure in [QAW-10, $x = 0$] that results in a greater number of grain boundaries per unit volume in the WZ.

Quantification of rupture stresses and strains

Table 3 shows the average values of rupture stress (σ_{rup}) and strain (ε_{rup}) for all conditions evaluated in this work. Among all the welding conditions, none of the samples ruptured in or near the WZ, indicating that the extremely refined grains contribute to increasing joint strength (Montecinos and Cuniberti, 2014; Sutou et al., 2005). The reference presented the lowest values for σ_{rup}, with an ε_{rup} close to that of the welded samples. As the samples do not present microstructural homogeneity and were subjected to unknown stress and temperature fields during CDFW, the detailed analysis of the behavior under tension becomes a difficult task and, therefore, will not be addressed in this work.

[QAW-10] presented the highest σ_{rup} and deviation in relation to the reference, around 25 % higher. This behavior is associated with the presence of a very refined microstructure (VHC de Albuquerque et al., 2010) that occupies approximately 20 % of the total length of the sample. [QAW-5] showed an increase of ~15 % in the σ_{rup} compared to the reference. High anisotropy and high GS are important characteristics that justify this behavior (Xie et al., 2015; Cissé and Asle Zaeem, 2021).

Table 3
Rupture stress (σ_{rup}) and rupture strain (ε_{rup}) of Cu-11.8Al-0.45Be (wt.%) SMA welded by CDFW.

	Reference	WAQ-10	WAQ-5	QAW-10	QAW-5
σ_{rup} (MPa)	247.1 ± 25.8	291.6 ± 44.0	280.1 ± 35.5	308.3 ± 76.0	283.9 ± 37.1
ε_{rup} (%)	11.2 ± 2.1	11.4 ± 1.1	10.3 ± 1.3	12.2 ± 1.4	11.3 ± 3.2

For conditions [WAQ-10] and [WAQ-5], deeper investigations need to be carried out, but the residual stresses along the TMAZ and the presence of extremely refined grains in the WZ may be responsible for the increase in the order of 18 and 13.4 %, respectively, in the σ_{rup} in relation to the reference (da Silva Andrade et al., 2021; Montecinos and Cuniberti, 2014).

The stress-strain curve for each condition is shown in Fig. 12. The first stage of loading can be understood as the elastic response of the martensite whose yield strength corresponds to the last stress value over the linear region. The reference presented the lowest yield strength and σ_{rup} probably associated with high GS, crystallographic defects, and high elastic anisotropy (Xie et al., 2015). The second linear part of the loading is directly linked to the reorientation of martensite variants and plastic deformation.

The sample welded in the martensitic state [WAQ-10] presents a slope of the second linear part of the curve slightly higher than that of the reference and considerably greater than that of the [QAW] condition. The presence of plastic deformation tends to increase the slope of this part of the curve (Montecinos and Cuniberti, 2008; Moghaddam et al., 2013). Therefore, the higher HV values between ±8 mm and the greater slope of the second linear part of the curve (stress *x* strain) in the sample [WAQ-10] reinforce the hypothesis of residual stresses close to WZ in this condition. However, the presence of γ_2 can also interfere minimally with the increase in the slope of the curve, but this will only be relevant for high volumetric fractions of this phase (Cuniberti et al., 2009).

Conclusions

The microstructural and thermomechanical characterizations were carried out on the Cu11.8Al0.45Be SMA welded by continuous drive rotary friction with different process parameters. It was found that the increase in friction pressure and the metallurgical state is fundamentally important in reducing the time required for welding. At the two friction pressures studied in this work, it is possible to verify the maintenance of

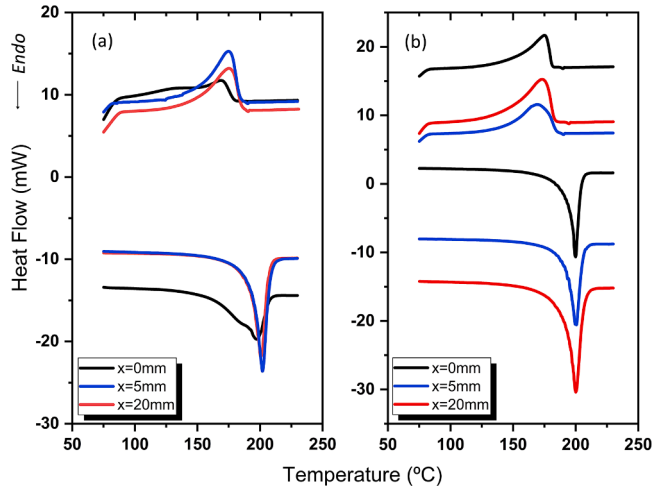

Fig. 11. DSC thermograms for [WAQ-10] (a), and [WAQ-5] (b) at $x = 0$ (WZ), $x = 5$ and $x = 20$ mm.

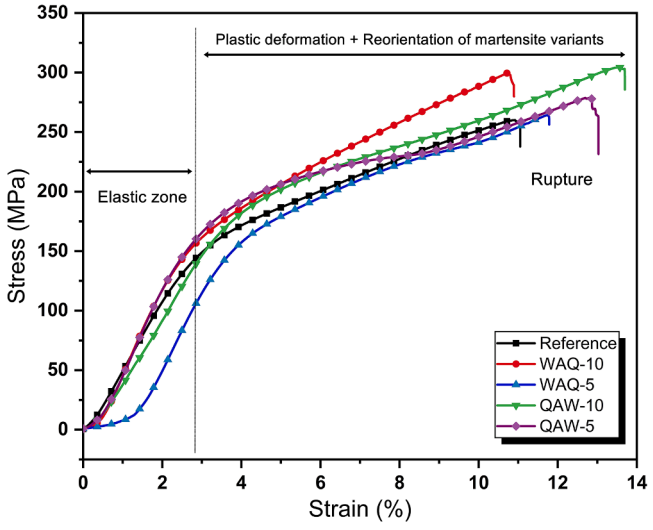

Fig. 12. Stress-strain curves for the base metal and samples welded by CDFW.

the martensitic transformation throughout the welded assembly, including in the welding zone. A slight increase in the tensile strength of the welded assembly compared to the base metal without major variations in microhardness was verified. Thus, it is possible to ensure that CDFW produces highly efficient joints, even in cases where the parts to be welded already have the SME, without compromising the functional properties of the material. The small time required for welding and the use of simple equipment makes the technique attractive, especially for the industrial sector.

CRediT authorship contribution statement

A.A.de Albuquerque: Writing – original draft, Methodology, Formal analysis, Conceptualization. **H. Louche:** Writing – review & editing, Formal analysis. **D.F.de Oliveira:** Writing – review & editing, Writing – original draft, Methodology, Formal analysis. **I.C.A. Brito:** Writing – review & editing, Writing – original draft, Supervision, Project administration, Methodology, Formal analysis, Conceptualization.

Declaration of competing interest

None.

Data availability

Data will be made available on request.

References

Abburi, N.R., Dixit, U.S., 2006. A knowledge-based system for the prediction of surface roughness in turning process. Robot. Comput. Integr. Manuf. 22, 363–372. https://doi.org/10.1016/j.rcim.2005.08.002.

Andrade, U., Meyers, M.A., Vecchio, K.S., Chokshi, A.H., 1994. Dynamic recrystallization in high-strain, high-strain-rate plastic deformation of copper. Acta Metal. Mater. 42, 3183–3195. https://doi.org/10.1016/0956-7151(94)90417-0.

Ates, H., Turker, M., Kurt, A., 2007. Effect of friction pressure on the properties of friction welded MA956 iron-based superalloy. Mater. Des. 28, 948–953. https://doi.org/10.1016/j.matdes.2005.09.015.

Bahador, A., Umeda, J., Tsutsumi, S., Hamzah, E., Yusof, F., Fujii, H., et al., 2019. Asymmetric local strain, microstructure and superelasticity of friction stir welded Nitinol alloy. Mater. Sci. Eng. A 767. https://doi.org/10.1016/j.msea.2019.138344.

Canbay, C.A., Karaduman, O., Ünlü, N., Özkul, İ., 2020. An exploratory research of calorimetric and structural shape memory effect characteristics of Cu–Al–Sn alloy. Physica B Condens. Matter 580. https://doi.org/10.1016/j.physb.2019.411932.

Canbay, C.A., Karaduman, O., Ünlü, N., Özkul, I., 2021. Study on basic characteristics of CuAlBe shape memory alloy. Braz. J. Phys. 51, 13–18. https://doi.org/10.1007/s13538-020-00823-1.

Chentouf, S.M., Bouabdallah, M., Cheniti, H., Eberhardt, A., Patoor, E., Sari, A., 2010. Ageing study of Cu-Al-Be hypoeutectoid shape memory alloy. Mater. Charact. 61, 1187–1193. https://doi.org/10.1016/j.matchar.2010.07.009.

Cissé, C., Asle Zaeem, M., 2021. Transformation-induced fracture toughening in CuAlBe shape memory alloys: a phase-field study. Int. J. Mech. Sci. 192 https://doi.org/10.1016/j.ijmecsci.2020.106144.

Cuniberti, A., Montecinos, S., Lovey, F.C., 2009. Effect of γ2-phase precipitates on the martensitic transformation of a β-CuAlBe shape memory alloy. Intermetallics. (Barking) 17, 435–440. https://doi.org/10.1016/j.intermet.2008.12.001.

Damodaram, R., Raman, S.G.S., Rao, K.P., 2013. Microstructure and mechanical properties of friction welded alloy 718. Mater. Sci. Eng. A 560, 781–786. https://doi.org/10.1016/j.msea.2012.10.035.

Del Sol, I., Rivero, A., Gamez, A.J., 2019. Effects of machining parameters on the quality in machining of aluminium alloys thin plates. Metals. (Basel) 9. https://doi.org/10.3390/met9090927.

Dunne, D., Morin, M., Gonzalez, C., Guenin, G., 2004. The effect of quenching treatment on the reversible martensitic transformation in CuAlBe alloys. Mater. Sci. Eng. A 378, 257–262. https://doi.org/10.1016/J.MSEA.2003.11.079.

Feng, A.H., Ma, Z.Y., 2009. Microstructural evolution of cast Mg-Al-Zn during friction stir processing and subsequent aging. Acta Mater. 57, 4248–4260. https://doi.org/10.1016/j.actamat.2009.05.022.

Freudenberger, J., Kauffmann, A., Klauß, H., Marr, T., Nenkov, K., Subramanya Sarma, V., et al., 2010. Studies on recrystallization of single-phase copper alloys by resistance measurements. Acta Mater. 58, 2324–2329. https://doi.org/10.1016/j.actamat.2009.12.018.

Fukumoto, S., Inoue, T., Mizuno, S., Okita, K., Tomita, T., Yamamoto, A., 2010. Friction welding of TiNi alloy to stainless steel using Ni interlayer. Sci. Technol. Weld. Joining 15, 124–130. https://doi.org/10.1179/136217109×12577814486692.

Grant, B., Preuss, M., Withers, P.J., Baxter, G., 2009. Rowlson M. Finite element process modelling of inertia friction welding advanced nickel-based superalloy. Mater. Sci. Eng. A 513–514, 366–375. https://doi.org/10.1016/j.msea.2009.02.005.

Huang, K., Logé, R.E., 2016. A review of dynamic recrystallization phenomena in metallic materials. Mater. Des. 111, 548–574. https://doi.org/10.1016/j.matdes.2016.09.012.

Kaouache, B., Berveiller, S., Inal, K., Eberhardt, A., Patoor, E., 2004. Stress analysis of martensitic transformation in Cu-Al-Be polycrystalline and single-crystalline shape memory alloy. Mater. Sci. Eng. A 378, 232–237. https://doi.org/10.1016/j.msea.2003.10.348.

Karadge, M., Preuss, M., Withers, P.J., Bray, S., 2008. Importance of crystal orientation in linear friction joining of single crystal to polycrystalline nickel-based superalloys. Mater. Sci. Eng. A 491, 446–453. https://doi.org/10.1016/j.msea.2008.04.064.

Kuo, H.H., Wang, W.H., Hsu, Y.F., 2006. Microstructural characterization of precipitates in Cu–10wt.%Al–0.8wt.%Be shape-memory alloy. Mater. Sci. Eng. A 430, 292–300. https://doi.org/10.1016/j.msea.2006.05.061.

Kök, M., Ata, Ş., Yakıncı, Z.D., Aydoğdu, Y., 2018. Examination of phase changes in the CuAl high-temperature shape memory alloy with the addition of a third element. J. Therm. Anal. Calorim. 133, 845–850. https://doi.org/10.1007/s10973-018-7176-0.

Li, W., Vairis, A., Preuss, M., Ma, T., 2016. Linear and rotary friction welding review. Int. Mater. Rev. 61, 71–100. https://doi.org/10.1080/09506608.2015.1109214.

Mani Prabu, S.S., Madhu, H.C., Perugu, C.S., Akash, K., Ajay Kumar, P., Kailas, S.V., et al., 2017. Microstructure, mechanical properties and shape memory behaviour of friction stir welded nitinol. Mater. Sci. Eng. A 693, 233–236. https://doi.org/10.1016/j.msea.2017.03.101.

Mani Prabu, S.S., Perugu, C.S., Madhu, H.C., Jangde, A., Khan, S., Jayachandran, S., et al., 2019. Exploring the functional and corrosion behavior of friction stir welded NiTi shape memory alloy. J. Manuf. Process. 47, 119–128. https://doi.org/10.1016/j.jmapro.2019.09.017.

Mazzer, E.M., Kiminami, C.S., Bolfarini, C., Cava, R.D., Botta, W.J., Gargarella, P., 2015. Thermodynamic analysis of the effect of annealing on the thermal stability of a Cu-Al-Ni-Mn shape memory alloy. Thermochim. Acta 608, 1–6. https://doi.org/10.1016/j.tca.2015.03.024.

Mazzer, E.M., Gargarella, P., Cava, R.D., Bolfarini, C., Galano, M., Kiminami, C.S., 2017. Effect of dislocations and residual stresses on the martensitic transformation of Cu-Al-Ni-Mn shape memory alloy powders. J. Alloy. Compd. 723, 841–849. https://doi.org/10.1016/j.jallcom.2017.06.312.

Moghaddam, A.O., Ketabchi, M., Bahrami, R., 2013. Kinetic grain growth, shape memory and corrosion behavior of two Cu-based shape memory alloys after thermomechanical treatment. Trans. Nonferrous Met. Soc. China (English Edition) 23, 2896–2904. https://doi.org/10.1016/S1003-6326(13)62812-5.

Montecinos, S., Cuniberti, A., 2008. Thermomechanical behavior of a CuAlBe shape memory alloy. J. Alloys Compd. 457, 332–336. https://doi.org/10.1016/j.jallcom.2007.03.077.

Montecinos, S., Cuniberti, A, 2014. Effects of grain size on plastic deformation in a β CuAlBe shape memory alloy. Mater. Sci. Eng. A 600, 176–180. https://doi.org/10.1016/j.msea.2014.02.028.

Oliveira, J.P., Miranda, R.M., Braz Fernandes, F.M., 2017. Welding and joining of NiTi shape memory alloys: a review. Prog. Mater. Sci. 88, 412–466. https://doi.org/10.1016/j.pmatsci.2017.04.008.

Oliveira, J.P., Zeng, Z., Berveiller, S., Bouscaud, D., Braz Fernandes, F.M., Miranda, R.M., et al., 2018. Laser welding of Cu-Al-Be shape memory alloys: microstructure and mechanical properties. Mater. Des. 148, 145–152. https://doi.org/10.1016/j.matdes.2018.03.066.

Ozbulut, O.E., Mir, C., Moroni, M.O., Sarrazin, M., Roschke, P.N., 2007. A fuzzy model of superelastic shape memory alloys for vibration control in civil engineering applications. Smart. Mater. Struct. 16, 818–829. https://doi.org/10.1088/0964-1726/16/3/031.

Pedrosa, M.T.M.A., Silva, D.D.S., Brito, I.C.A., Alves, R.F., Caluête, R.E., Gomes, R.M., et al., 2022. Effects of hot rolling on the microstructure, thermal and mechanical properties of CuAlBeNbNi shape memory alloy. Thermochim. Acta 711. https://doi.org/10.1016/j.tca.2022.179188.

Ponweiser, N., Lengauer, C.L., Richter, K.W., 2011. *Re*-investigation of phase equilibria in the system Al-Cu and structural analysis of the high-temperature phase η1-Al 1-δCu. Intermetallics. (Barking) 19, 1737–1746. https://doi.org/10.1016/j.intermet.2011.07.007.

Prabu, S.S.M., Aravindan, S., Ghosh, S., Palani, I.A., 2023. Solid-state welding of nitinol shape memory alloys: a review. Mater. Today Commun. 35 https://doi.org/10.1016/j.mtcomm.2023.105728.

Preuss, M., da Fonseca, J.Q., Steuwer, A., Wang, L., Withers, P.J., Bray, S., 2004. Residual stresses in linear friction welded IMI550. J. Neutron Res. 12, 165–173. https://doi.org/10.1080/10238160410001734630.

Priymak, E., Boumerzoug, Z., Stepanchukova, A., Ji, V., 2020. Residual stresses and microstructural features of rotary-friction-welded from dissimilar medium carbon steels. Phys. Met. Metallogr. 121, 1339–1346. https://doi.org/10.1134/S0031918×20130165.

Pushin, V.G., Kuranova, N.N., Svirid, A.E., Uksusnikov, A.N., Ustyugov, Y.M., 2022. Design and development of high-strength and ductile ternary and multicomponent eutectoid Cu-based shape memory alloys: problems and perspectives. Metals. (Basel) 12. https://doi.org/10.3390/met12081289.

Qehaja, N., Jakupi, K., Bunjaku, A., Bruçi, M., Osmani, H., 2015. Effect of machining parameters and machining time on surface roughness in dry turning process. Procedia Eng. 100, 135–140. https://doi.org/10.1016/j.proeng.2015.01.351. Elsevier Ltd.

Ramesh Kumar, R., Babu, J.M., Saleh, B., Fayaz, H., Chandrashekar, A., Gera, T., et al., 2023. Experimental and analytical investigation on friction welding dissimilar joints for aerospace applications. Ain Shams Eng. J. 14 https://doi.org/10.1016/j.asej.2022.101853.

Rehman, A.U., Babu, N.K., Talari, M.K., Usmani, Y., Alkhalefah, H., 2021a. Characterisation of microstructure and mechanical properties of linear friction welded α+β titanium alloy to nitinol. Appl. Sci. (Switzerland) 11. https://doi.org/10.3390/app112210680.

Rehman, A.U., Babu, N.K., Talari, M.K., Usmani, Y.S., Al-Khalefah, H, 2021b. Microstructure and mechanical properties of dissimilar friction welding ti-6al-4v alloy to nitinol. Metals. (Basel) 11, 1–11. https://doi.org/10.3390/met11010109.

Rehman, A.U., Babu, N.K., Talari, M.K., Usmani, Y.S., Al-Khalefah, H, 2021c. Microstructure and mechanical property correlation between rotary friction welded nitinol–nitinol joints. Front. Mater. 8 https://doi.org/10.3389/fmats.2021.726383.

Roca, P.L., Isola, L., Vermaut, P., Malarría, J, 2017. Relationship between grain size and thermal hysteresis of martensitic transformations in Cu-based shape memory alloys. Scr. Mater. 135, 5–9. https://doi.org/10.1016/j.scriptamat.2017.03.016.

Sampath, V., Srinithi, R., Santosh, S., Sarangi, P.P., Fathima, J.S., 2020. The effect of quenching methods on transformation characteristics and microstructure of an NiTiCu shape memory alloy. Trans. Indian Inst. Met. 73, 1481–1488. https://doi.org/10.1007/s12666-020-01909-9.

Sampath, V., 2005. Studies on the effect of grain refinement and thermal processing on shape memory characteristics of Cu-Al-Ni alloys. Smart Mater. Struct. 14 https://doi.org/10.1088/0964-1726/14/5/013 vol.

Sedlaček, M., Podgornik, B., Vižintin, J., 2009. Influence of surface preparation on roughness parameters, friction and wear. Wear 266, 482–487. https://doi.org/10.1016/j.wear.2008.04.017.

Shinoda, T., Tsuchiya, T., Takahashi, H., 1992. Friction welding of shape memory alloy. Weld. Int. 6, 20–25. https://doi.org/10.1080/09507119209548136.

Shinoda, T., Owa, T., Magula, V., 1999. Microstructural analysis of friction welded joints in TiNi alloy. Weld. Int. 13, 180–185. https://doi.org/10.1080/09507119909447361.

Silva, D.D.S., Vieira, R.T., Falcão, G.M.S., Brito, I.C.A., Caluête, R.E., Gomes, R.M., et al., 2023. New insights into the effects of solidification process on the thermodynamic parameters and mechanical properties of CuAlBeNbNi shape memory alloy. J. Mater. Res. Technol. 24, 4329–4335. https://doi.org/10.1016/j.jmrt.2023.04.053.

Sun, Q., Aslan, A., Li, M., Chen, M., 2014. Effects of grain size on phase transition behavior of nanocrystalline shape memory alloys. Sci. China Technol. Sci. 57, 671–679. https://doi.org/10.1007/s11431-014-5505-5.

Sutou, Y., Omori, T., Yamauchi, K., Ono, N., Kainuma, R., Ishida, K., 2005. Effect of grain size and texture on pseudoelasticity in Cu-Al-Mn-based shape memory wire. Acta Mater. 53, 4121–4133. https://doi.org/10.1016/j.actamat.2005.05.013.

Taheri, H., Kilpatrick, M., Norvalls, M., Harper, W.J., Koester, L.W., Bigelow, T., et al., 2019. Investigation of nondestructive testing methods for friction stirwelding. Metals. (Basel) 9. https://doi.org/10.3390/met9060624.

Turner, R., Ward, R.M., March, R., Reed, R.C., 2012. The magnitude and origin of residual stress in Ti-6Al-4V linear friction welds: an investigation by validated numerical modeling. Metal. Mater. Trans. B 43, 186–197. https://doi.org/10.1007/s11663-011-9563-9. Process Metallurgy and Materials Processing Science.

Uday, M.B., Fauzi, M.N.A., Zuhailawati, H., Ismail, A.B., 2010. Advances in friction welding process: a review. Sci. Technol. Weld. Joining 15, 534–558. https://doi.org/10.1179/136217110×12785889550064.

Vairis, A., Papazafeiropoulos, G., Tsainis, A.M., 2016. A comparison between friction stir welding, linear friction welding and rotary friction welding. Adv. Manuf. 4, 296–304. https://doi.org/10.1007/s40436-016-0163-4.

Vyas, H.D., Mehta, K.P., Badheka, V., Doshi, B., 2022. Microstructure evolution and mechanical properties of continuous drive friction welded dissimilar copper-stainless steel pipe joints. Mater. Sci. Eng. A 832. https://doi.org/10.1016/j.msea.2021.142444.

West, P., Shunmugasamy, V.C., Usman, C.A., Karaman, I., Mansoor, B., 2021. Part I.: friction stir welding of equiatomic nickel titanium shape memory alloy – microstructure, mechanical and corrosion behavior. J. Adv. Joining Process. 4, 100071 https://doi.org/10.1016/j.jajp.2021.100071.

Xie, J.X., Liu, J.L., Huang, H.Y., 2015. Structure design of high-performance Cu-based shape memory alloys. Rare Metals 34, 607–624. https://doi.org/10.1007/s12598-015-0557-7.

Zhang, K., Qian, X., Chen, J., Chen, J., Lu, H., 2022. Non-monotonic evolution of microstructure and fatigue properties of round bar–plate rotary friction welding joints in 304 austenitic stainless steel. Mater. Des. 224 https://doi.org/10.1016/j.matdes.2022.111400.

Zhang, Y., Xu, L., Zhao, L., Lin, D., Liu, M., Qi, X., et al., 2023. Process-microstructure-properties of CuAlNi shape memory alloys fabricated by laser powder bed fusion. J. Mater. Sci. Technol. 152, 1–15. https://doi.org/10.1016/J.JMST.2022.12.037.

Zu, X.T., Wang, L.M., Huo, Y., Lin, L.B., Wang, Z.G., Lu, T.C., et al., 2002. Effect of electron irradiation on the transformation characteristics of narrow hysteresis TiNiCu shape memory alloys. Appl. Phys. Lett. 80, 31–33. https://doi.org/10.1063/1.1427747.

da Paz, J.S., de Oliveira, D.F., Brito, I.C.A., Caluête, R.E., de Souza Falcão, G.M., Gomes, R.M., 2022. Development of smart fasteners for joining metal sheets. MRS Commun. 12, 329–335. https://doi.org/10.1557/s43579-022-00180-x.

da Silva Andrade, B.H., de Souza Falcão, G.M., Brito, I.C.A., Caluête, R.E., Gomes, R.M., de Oliveira, D.F., 2021. Effects of annealing temperature on thermodynamic parameters and mechanical properties of a Cu-Al-Be-Nb-Ni-Cr alloy. Mater. Lett. 302, 2–5. https://doi.org/10.1016/j.matlet.2021.130390.

de Albuquerque, V.H.C., Melo TA de, A., Gomes, R.M., de Lima, S.J.G., Tavares, J.M.R.S, 2010a. Grain size and temperature influence on the toughness of a CuAlBe shape memory alloy. Mater. Sci. Eng. A 528, 459–466. https://doi.org/10.1016/j.msea.2010.09.034.

de Albuquerque, V.H.C., Melo TA de, A., de Oliveira, D.F., Gomes, R.M., Tavares, J.M.R.S, 2010b. Evaluation of grain refiners influence on the mechanical properties in a CuAlBe shape memory alloy by ultrasonic and mechanical tensile testing. Mater. Des. 31, 3275–3281. https://doi.org/10.1016/j.matdes.2010.02.010.

de Oliveira, D.F., Brito, I.C.A., França, F.J.C., de Lima, S.J.G., Mello, T.A.A., Gomes, R.M., 2017. Assessment of pipe coupling by using the recovery of stress-induced martensites in superelastic Cu-11.8Al-0.6Be-0.5Nb alloy. J. Mater. Eng. Perform. 26, 2264–2270. https://doi.org/10.1007/s11665-017-2647-1.